

Effective Complex Permittivity of Random Composites

Dominique Jeulin, L. Savary

▶ **To cite this version:**

Dominique Jeulin, L. Savary. Effective Complex Permittivity of Random Composites. Journal de Physique I, 1997, 7 (9), pp.1123-1142. 10.1051/jp1:1997103 . jpa-00247386

HAL Id: jpa-00247386
https://hal.science/jpa-00247386

Submitted on 4 Feb 2008

HAL is a multi-disciplinary open access archive for the deposit and dissemination of scientific research documents, whether they are published or not. The documents may come from teaching and research institutions in France or abroad, or from public or private research centers.

L'archive ouverte pluridisciplinaire **HAL**, est destinée au dépôt et à la diffusion de documents scientifiques de niveau recherche, publiés ou non, émanant des établissements d'enseignement et de recherche français ou étrangers, des laboratoires publics ou privés.

J. Phys. I France 7 (1997) 1123–1142 SEPTEMBER 1997, PAGE 1123

Effective Complex Permittivity of Random Composites

D. Jeulin (*) and L. Savary

CMM, ENSMP, 35 Rue St-Honoré, 77305 Fontainebleau, France

(Received 20 February 1997, revised 21 April 1997, accepted 26 May 1997)

PACS.02.50.-r – Probability theory, stochastic processes, and statistics
PACS.72.80.Tm – Composite materials
PACS.78.20.Bh – Theory, models, and numerical simulation

Abstract. — The prediction of the macroscopic complex permittivity of composites is based on the derivations of D.J. Bergman and G. Milton, by means of third order correlation functions. This approach is applied to morphological models of textures simulating the geometry of two phase composites: random mosaics built on a random tessellation, Boolean models, Dead Leaves models, or combinations of these models into hierarchical random textures; they allow us to look for optimal textures with respect to the material behaviour.

1. Introduction

Modeling composite microstructures by means of random sets [1–6] is a useful way to summarize microstructural information and to propose practical methods of simulation. For some models, probabilistic properties such as correlation functions are available. This enables an estimation of the overall properties of random composites from bounds based on a limited amount of statistical information [7, 8]. The bounds that are commonly used for isotropic media are Hashin and Shtrikman (H-S) bounds based on volume fractions [9]. Tighter bounds can be derived from additional statistical information, such as the infinite set of their correlation functions [7, 8, 10]. In practice, useful bounds are obtained by limiting the calculations to the third order.

In this presentation, we recall the third and fourth order bounds obtained for two-phase media with a complex permittivity [11, 12]; then we introduce some basic random sets models, and their combination to produce hierarchical textures. For each model is given its three-point function $\zeta_1(p)$ defined below. This is useful to compare the incidence of the morphology of random media on their overall physical properties, as illustrated in the last part. In the present case, this can be applied to the prediction of optical properties of composites (and of their change according to the frequency ω). This is limited to the quasi-static case, where the light wavelength is much larger than the scale of microstructural heterogeneities. Earlier attempts were made to deduce geometrical information from these bounds [13, 14]. A shorter presentation of our results is given in [15].

(*) Author for correspondence (e-mail: jeulin@cmm.ensmp.fr)

© Les Éditions de Physique 1997

2. Principle of Calculation of Complex Bounds

We consider random composites made of two phases A (with volume fraction p) and A^c (with volume fraction $q = 1 - p$). In the case of absorbing or conductive media, the dielectric permittivity depends on the frequency ω of the electric field and is complex: $\epsilon = \epsilon' - i\epsilon''$ (with $i^2 = -1$, ϵ' is the dielectric constant, and ϵ'' the dielectric loss factor). The bounds derived by Beran for real permittivity [16] are not available anymore.

The derivation of the bounds on the effective permittivity ϵ_e of a two-component composite with complex permittivity ϵ_1 (phase A) and ϵ_2 (phase A^c) [17] is based on the Bergman's method [18], which is valid in the quasi-static case (when the wavelength is much larger than the characteristic length of the microstructure). As did Milton, it is convenient to introduce the variable τ,

$$\tau = (\epsilon_1 + \epsilon_2)/(\epsilon_1 - \epsilon_2)$$

ϵ_e is expressed as a function of ϵ_2 and τ which can be represented in the following closed rational form [17],

$$\epsilon_e = \epsilon_2 \prod_{i=0}^{m} (\tau - \tau_i')/(\tau - \tau_i), \tag{1}$$

where the constants τ_i and τ_i' are real and must satisfy (2),

$$1 \geq \tau_0 > \tau_0' > \tau_1 > \tau_1' . \quad \tau_m' \geq -1. \tag{2}$$

In two dimensions, the poles and zeroes in $[0,1]$ define (by interchange) those in $[-1,0]$.

Using (1) and the method described in [17], the Beran's bounds can be generalized to the complex plane (ϵ', ϵ''). The bounds for complex ϵ_1 and ϵ_2 restrict ϵ_e to a region Ω^n of the complex plane which depends on what is known about the microstructure of the composite material. They depend on some constants R_n, calculated from the perturbation expansion of ϵ_e [16], and summarizing the microstructural information on the composite:

$$R_n = \left. \frac{\partial^n \epsilon_e(\epsilon_1, \epsilon_2)}{\partial \epsilon_1^n} \right|_{\epsilon_1 = \epsilon_2 = 1} \tag{3}$$

These constants R_n are:

- $R_1 = p$ for any composite material;
- $R_2 = -2pq/d$ if the material is statistically isotropic in $\mathbb{R}^d$ (with $d = 2, 3$);
- $R_3 = \frac{d+1}{d} pq(\zeta_1 + \frac{q}{d-1})$ (with $d = 2, 3$) where the Milton's function ζ_1 is calculated from the 3 points correlation function;
- $R_4 = 3pq^2(1 + q) - 2R_3(1 + 2q)$ for statistically isotropic 2-dimensional materials. For this type of material Keller [19], Dykhne [20] and Mendelson [21] have shown that

$$\epsilon_e(\epsilon_1, \epsilon_2)\epsilon_e(\epsilon_2, \epsilon_1) = \epsilon_1 \epsilon_2. \tag{4}$$

It was observed by Milton [11] that (4) implies the given relation between R_3 and R_4.

For higher values of n, R_n can be calculated in terms of higher-order correlation functions. When the constants τ_i and τ_i' are allowed to vary subject to the appropriate restrictions (2) and (3), while keeping τ, ϵ_2, and R_n $(n = 1, 2, .., J)$ fixed [11, 12, 17, 18], ϵ_e, given by equation (1), covers the domains Ω^n of the complex plane. The larger the morphological information taken into account, the smaller is this region which provides rigorous bounds on ϵ_e.

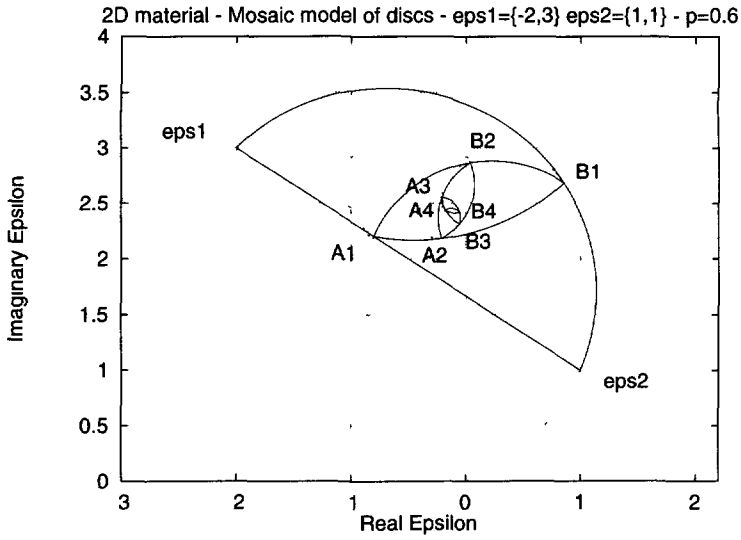


Fig. 1. — Construction of the regions Ω^n (for $n = 0, .., 4$).

The Milton's function $\zeta_1(p)$ [12] entering into the calculation of R_3 and R_4 is defined below (Eq. (5)). It is known for some theoretical random set models or can be calculated from measurements obtained by image analysis. It is deduced from the probability $P(h_1, h_2)$ that the three points $\{x\}$, $\{x + h_1\}$, $\{x + h_2\}$ belong to A_1 (with volume fraction p). Denoting this probability $P(|h_1|, |h_2|, \theta)$, with $u = \cos\theta$, θ being the angle between the vectors h_1 and h_2, we have:

$$\zeta_1(p) = \frac{9}{4pq} \int_0^{+\infty} \frac{\mathrm{d}x}{x} \int_0^{+\infty} \frac{\mathrm{d}y}{y} \int_{-1}^{+1} (3u^2 - 1) P(x, y, \theta)\, \mathrm{d}u \text{ in three dimensions}$$

$$\zeta_1(p) = \frac{4}{\pi pq} \int_0^{+\infty} \frac{\mathrm{d}x}{x} \int_0^{+\infty} \frac{\mathrm{d}y}{y} \int_0^{\pi} P(x, y, \theta) \cos(2\theta)\, \mathrm{d}\theta \text{ in two dimensions.} \tag{5}$$

Exchanging phases A and A^c enables us to define the function $\zeta_2(q)$ with $\zeta_2(q) = 1 - \zeta_1(p)$. The function $\zeta_1(p)$ satisfies the inequalities $0 \leq \zeta_1(p) \leq 1$.

Now, let us remind how bounds are constructed.

The regions $\Omega, \Omega^1, \Omega^2, \Omega^3$, and Ω^4 are obtained by the geometric constructions shown in Figure 1. The bounds always restrict ϵ_e to a region of the complex plan enclosed by circular arcs (the pair of arcs $A^nB^nA^{n-1}$ and $A^nB^nB^{n-1}$ bound Ω^n). Given ϵ_1, ϵ_2, p_1, d and ζ_1, the points A^n and B^n (for $n = 1$, 2, 3 et 4) are first plotted.

- Without any information on the geometry, ϵ_e is confined to the region $\Omega(\epsilon_1, \epsilon_2)$ of the complex plane (ϵ', ϵ'') bounded by the arc $O\epsilon_1\epsilon_2$ and the straight line $\epsilon_1\epsilon_2$ [17].

- Knowing the volume fractions of the components p and $q = 1 - p$, ϵ_e is confined to a smaller region $\Omega^1(\epsilon_1, \epsilon_2; p, q)$, which is bounded by the two circular arcs $A^1B^1\epsilon_1$ and $A^1B^1\epsilon_2$ [17].

$$\begin{cases} A^1 = p\epsilon_1 + q\epsilon_2 \\ B^1 = (p/\epsilon_1 + q/\epsilon_2)^{-1} \end{cases}.$$

- For a statistically isotropic structure, ϵ_e is confined to a smaller region $\Omega^2(\epsilon_1, \epsilon_2; p, q; d)$ of the complex plane ($d = 2$ or 3), bounded by the two circular arcs $A^2B^2A^1$ and $A^2B^2B^1$ [17].

$$\begin{cases} A^2 = \epsilon_1 + \dfrac{dq\epsilon_1(\epsilon_2 - \epsilon_1)}{d\epsilon_1 + p(\epsilon_2 - \epsilon_1)} \\ \\ B^2 = \epsilon_2 + \dfrac{dp\epsilon_2(\epsilon_1 - \epsilon_2)}{d\epsilon_2 + q(\epsilon_1 - \epsilon_2)} \end{cases}$$

- Knowing the Milton's function ζ_1, the region $\Omega^3(\epsilon_1, \epsilon_2; p, q; d; \zeta_1, \zeta_2)$ can be defined for $d = 2$ or 3; it is bounded by the two circular arcs $A^3B^3A^2$ and $A^3B^3B^2$ [12,22].

$$\begin{cases} A^3 = \epsilon_1 \dfrac{1 + ((d-1)(1+q) + \zeta_1 - 1)\beta_{21} + (d-1)((d-1)q + \zeta_1 - 1)\beta_{21}^2}{1 - (q + 1 - \zeta_1 - (d-1))\beta_{21} + ((q - (d-1)p)(1-\zeta_1) - (d-1)q)\beta_{21}^2} \\ \\ B^3 = \epsilon_2 \dfrac{1 + ((d-1)(p+\zeta_1) - 1)\beta_{12} + (d-1)(((d-1)p - q)\zeta_1 - p)\beta_{12}^2}{1 - (1 + p - (d-1)\zeta_1)\beta_{12} + (p - (d-1)\zeta_1)\beta_{12}^2} \end{cases}$$

with $\beta_{ij} = \dfrac{\epsilon_i - \epsilon_j}{\epsilon_i + (d-1)\epsilon_j}$

The range A^3–B^3 is of the order of $(\epsilon_1 - \epsilon_2)^4$.

- In the case of a two-dimensional material, fourth order bounds can be defined. The region $\Omega^4(\epsilon_1, \epsilon_2; p, q; d = 2; \zeta_1, \zeta_2)$ is bounded by the two arcs $A^4B^4A^3$ and $A^4B^4B^3$ [12].

$$\begin{cases} A^4_{d=2} = \epsilon_1 \dfrac{1 + q\beta_{21} - p\zeta_2\beta_{21}^2}{1 - q\beta_{21} - p\zeta_2\beta_{21}^2} \\ \\ B^4_{d=2} = \epsilon_2 \dfrac{1 - p\beta_{21} - q\zeta_1\beta_{21}^2}{1 + p\beta_{21} - q\zeta_1\beta_{21}^2} \end{cases}$$

The range A^4–B^4 is of the order of $(\epsilon_1 - \epsilon_2)^5$.

Figure 1 shows the effect of the order of the approximation of the effective permittivity ϵ_e, for a two phase composite with $p = 0.6$ (volume fraction of phase 1). In this example and in the following sections, we use the same values for the permittivity of ϵ_1 and ϵ_2 as in [17]:

$$\begin{cases} \textit{phase 1} \text{ corresponds to } \epsilon_1 = -2 + 3i \\ \textit{phase 2} \text{ corresponds to } \epsilon_2 = 1 + i \end{cases}$$

3. Real Dielectric Permittivity, Optimal Textures, and Limitations of the Method

When ϵ_1 and ϵ_2 are both real and positive, the bounds reduce to those obtained by Wiener, Hashin and Shtrikman, Beran and Milton, points A^z and B^z giving lower and upper bounds respectively: all the regions Ω^n become segments on the real axis. For $\zeta_1(p) = 1$ or 0 (and only in these cases), the two bounds obtained in the case of a real permittivity coincide and are equal to the H-S upper ($\zeta_1(p) = 1$) or lower ($\zeta_1(p) = 0$) bound. For given p, ϵ_1 and ϵ_2 (with $\epsilon_1 > \epsilon_2$), the two bounds increase with the function $\zeta_1(p)$ (while the H-S bounds remain fixed), so that higher values of the effective properties are expected. This point is used

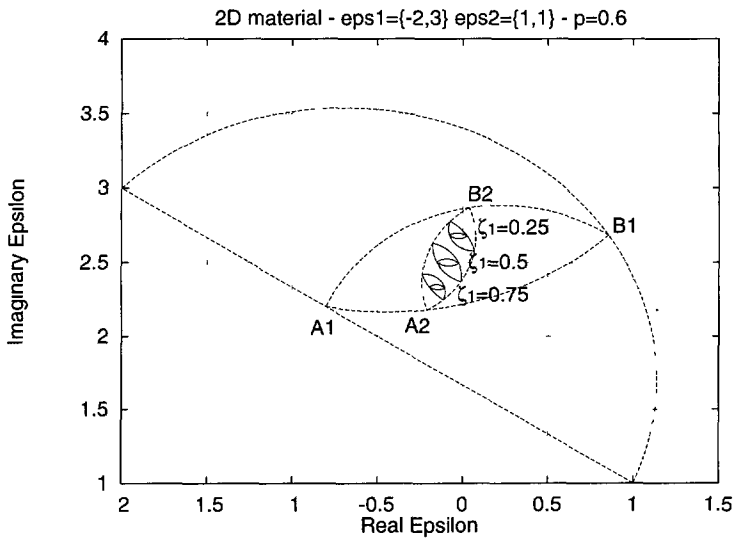


Fig. 2. — Position of the regions Ω^3 and Ω^4 (3rd and 4th order bounds) when the function ζ_1 changes ($\zeta_1 = 0.25 - 0.5 - 0.75$).

to compare the expected properties of materials with different morphologies, and to design optimal morphologies [23,24].

For the case of a complex permittivity, the third and fourth order regions move from the point A^2 to the point B^2 when ζ_1 changes from 1 to 0 (Fig. 2); given the properties of the two phases (ϵ_1 and ϵ_2), and possibly their volume fraction, a random texture can be looked for, from the desired value of ϵ_e, and consequently of ζ_1.

This approach can be successful when the domains corresponding to different textures are confined and do not overlap too much. This happens for a limited contrast of permittivity, or for some particular relative positions of the three starting points (O, ϵ_1, ϵ_2) of the geometric construction of the regions Ω^n in the complex plane. If the angle between the complex dielectric constants of both phases $\widehat{\epsilon_1 O \epsilon_2}$ is acute (which means $\epsilon_1' \epsilon_2' + \epsilon_1'' \epsilon_2'' > 0$), the domain Ω is confined (Fig. 3), and so are the domains Ω^n. If this is not the case *i.e.* $\widehat{\epsilon_1 O \epsilon_2}$ is obtuse, the region Ω is very large (Fig. 4), and consequently, the regions Ω^n are not confined. This is a limitation of the method.

In Figure 5, we show a case for which the model cannot separate the two regions (even for 4th order bounds) obtained when exchanging the morphology of the two phases of a Boolean model of discs (see Sect. 4.1.2). The values $\epsilon_1 = \{-4.10, 0.37\}$ and $\epsilon_2 = \{1.93, 0\}$ correspond respectively to the permittivity of the following real materials [25] for a 6 eV energy electromagnetic wave:

phase 1: Ag (silver)
phase 2: MgF_2 (magnesium fluoride)

The angle $\widehat{\epsilon_1 O \epsilon_2}$ is very obtuse. The two domains Ω^4 are very large and overlap. A better separation of the domains would require higher order morphological information.

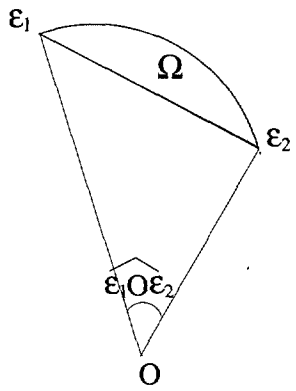


Fig. 3

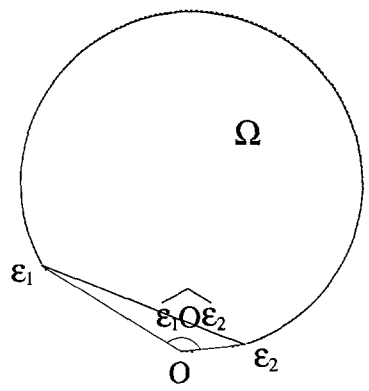


Fig. 4.

Fig. 3. — Construction of the domain Ω. The angle $\widehat{\epsilon_1 O \epsilon_2}$ is acute. The domain Ω is confined.

Fig. 4. — Construction of the domain Ω. The angle $\widehat{\epsilon_1 O \epsilon_2}$ is obtuse. The domain Ω is large.

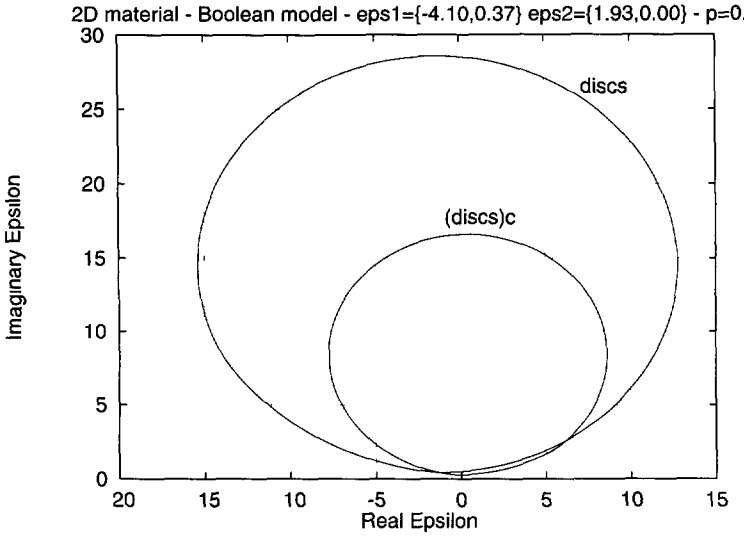


Fig. 5. — 4th order bounds Ω^4 for Boolean models of discs and $(\text{discs})^c$. Example where $\epsilon_1'\epsilon_2' + \epsilon_1''\epsilon_2'' < 0$: the regions are overlapping.

4. Examples of Random Sets Models

Random composites made of two phases A (with volume fraction p) and A^c (with volume fraction $q = 1 - p$) can be modelled by a stationary and isotropic random set A. Random sets models are characterized by the probability distributions $T(K)$ or $Q(K)$ defined on compact sets K:

$$T(K) = P\{K \cap A \neq \emptyset\} = P\{K \text{ hits } A\} \tag{6}$$

$$Q(K) = P\{K \subset A^c\} = 1 - T(K).$$

Particular cases of equation (6) give the covariance $Q(h) = P\{x \in \mathrm{A}^c, x+h \in \mathrm{A}^c\}$ when $\mathrm{K} = \{x, x+h\}$ and the three point probability $P\{x, y, \theta\}$ entering in equation (5) when $\mathrm{K} = \{x, x+h_1, x+h_2\}$. The theoretical expression of $T(\mathrm{K})$ or $Q(\mathrm{K})$ is available for various models. On the other hand, $T(\mathrm{K})$ or $Q(\mathrm{K})$ can be estimated from image analysis on pictures of the material. This is used to check the validity of a model, or to estimate its parameters.

In this section, we recall results for the function $\zeta_1(p)$ obtained for some random sets (or two-phase media) models noted A. More details are found in [23,24].

4.1. Basic Random Sets Models

4.1.1. The Mosaic Model. — The mosaic model [4–6,26], or "cell" model [27] is built in two steps: starting with a random tessellation of space into cells, every cell A′ is assigned independently to the random set A with the probability p and to A^c with the probability q. The medium is symmetric in A and A^c, which may be exchanged (changing p into q), and therefore $\zeta_1(0.5) = 0.5$. For the area fraction 0.5 in two dimensions, the Keller-Dykhne expression ($\epsilon_e = \sqrt{\epsilon_1 \epsilon_2}$) is satisfied, and would give the exact solution in the center of the bounds in Figure 1. For the mosaic model equation (5) becomes [12]:

$$\zeta_1(p) = p + a(q-p) \text{ with } a = \frac{d^2 G - 1}{d-1} \qquad \zeta_2(p) = \zeta_1(p) \tag{7}$$

and therefore $\zeta_1(p)$ varies linearly with the proportion p, with a slope $1-2a$ ($0 \le a \le 1$). In equation (7) the parameter G defined by Miller depends only on the random cell geometry by means of the function $s(|h_1|, |h_2|, \theta)$:

$$s(|h_1|, |h_2|, \theta) = \frac{\overline{\mu}_d(\mathrm{A}' \cap \mathrm{A}'_{h_1} \cap \mathrm{A}'_{h_2})}{\overline{\mu}_d(\mathrm{A}')}$$

where μ_d is the Lebesgue measure in $\mathbb{R}^d$, $\overline{\mu_d}$ its average over the realizations of A′, and A'_h is obtained by translation of A′ by the vector h. Then

$$G = \frac{1}{9} + \frac{1}{2} \int_0^{+\infty} \frac{\mathrm{d}x}{x} \int_0^{+\infty} \frac{\mathrm{d}y}{y} \int_{-1}^{+1} (3u^2 - 1) s(x, y, \theta)\, \mathrm{d}u \text{ in } \mathbb{R}^3$$

$$G = \frac{1}{4} + \frac{1}{\pi} \int_0^{+\infty} \frac{\mathrm{d}x}{x} \int_0^{+\infty} \frac{\mathrm{d}y}{y} \int_0^{+\pi} s(x, y, \theta) \cos(2\theta)\, \mathrm{d}\theta \text{ in } \mathbb{R}^2.$$

We have $1/9 \le G \le 1/3$ in three dimensions and $1/4 \le G \le 1/2$ in two dimensions. The two extreme cases are the following:

- $a = 0$ for $G = 1/9$ in $\mathbb{R}^3$ and for $G = 1/4$ in $\mathbb{R}^2$ (this corresponds to spherical and disc cells respectively),
- $a = 1$ for $G = 1/3$ in $\mathbb{R}^3$ and for $G = 1/2$ in $\mathbb{R}^2$ (corresponding to spheroidal cells of plate and needle shapes respectively).

A particular random mosaic (Fig. 6; the lines of the tessellation, which are shown on this figure for convenience, do not exist in the final structure) can be obtained from a Poisson tessellation of space by Poisson random planes in $\mathbb{R}^3$ (with the intensity λ, which is a scale

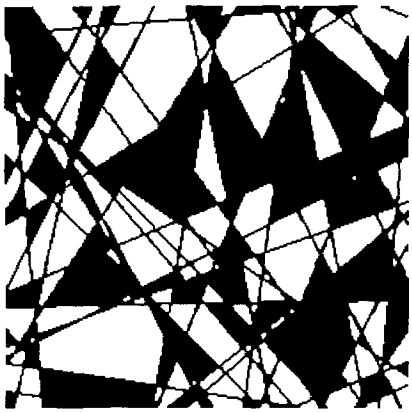


Fig. 6.

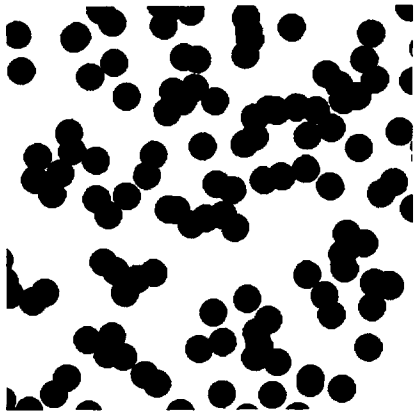


Fig. 7.

Fig. 6. — Mosaic model built on a Poisson tessellation.

Fig. 7. — Boolean model of discs.

parameter that does not appear in the calculation of G) and by Poisson lines in $\mathbb{R}^2$ [2,3]. The cells of this tessellation are Poisson polyhedra and Poisson polygons. For the Poisson cells built up from this tessellation, we have:

$$s(|h_1|, |h_2|, \theta) = \exp\left(-\lambda\left(|h_1| + |h_2| + \sqrt{|h_1|^2 + |h_2|^2 - 2|h_1||h_2|\cos\theta}\right)\right).$$

Therefore, G can be calculated analytically:

- $G = 1 - \ln 2$ [26], in $\mathbb{R}^2$ and we have $a = 3 - 4\ln 2$;
- $G = 1/6$ [23], in $\mathbb{R}^3$, and we have $a = 1/4$.

Anisotropic cells (but distributed with a uniform orientation) are studied in [24]. G (and consequently $\zeta_1(p)$ for $a \leq 1/2$) increases with the cell anisotropy: for example, for rectangles with $L = \text{length/width} = 200$, $G = 0.491$.

4.1.2. The Boolean Model . — The Boolean model [1,2] is obtained by implantation (with possible overlaps) of random primary grains A′ (discs are used for the two dimensional simulation of Fig. 7) on Poisson points x_k with the intensity λ (namely the average number of point per unit area or volume): $A = \cup_{x_k} A'_{x_k}$. For this model, we have:

$$Q(K) = \exp\left(-\lambda \overline{\mu}_d(A' \oplus \check{K})\right) = q^{\overline{\mu}_d(A' \oplus \check{K})/\overline{\mu}_d(A')}$$

where $A' \oplus \check{K} = \cup_{-x \in K} A'_x$ is the result of the dilation of A′ by K [3].

Any shape (convex or non convex, and even non connected) can be used for the grain A′. Most often in the literature, Boolean models of spheres are considered. Contrary to the mosaic model, the Boolean model is not symmetric, and therefore, different bounds are obtained when exchanging the properties of A and A^c. From numerical calculations [23, 24], it was found, with a good approximation, that linear functions of p are obtained for $\zeta_1(p)$: $\zeta_1(p) \simeq \alpha p + \beta$.

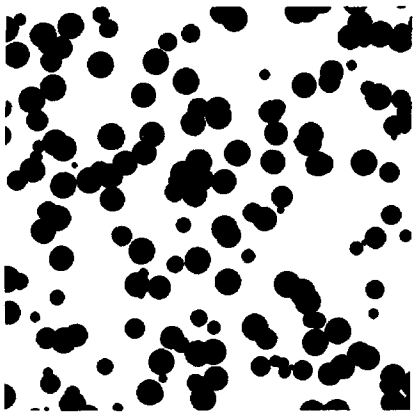


Fig. 8.



Fig. 9.

Fig. 8. — Section of a Boolean model of spheres.

Fig. 9. — Boolean model of Poisson polygons.

The function $\zeta_1(p)$ was estimated in [28,29] for spheres (Fig. 8) and in [23,24,30] for discs (Fig. 7). It is given in [23,24], for grains made of polygons in $\mathbb{R}^2$, including Poisson polygons (Fig. 9). These results (and $\zeta_2(p) = 1 - \zeta_1(1-p)$ obtained by exchange of the two phases) are summarized by:

$$\begin{gathered}
\zeta_1(p) \simeq 0.5615p \text{ for spheres [28,29]} \\
\zeta_2(p) \simeq 0.5615p + 0.4385 \text{ for (spheres)}^c \\
\zeta_1(p) \simeq \frac{2}{3}p \text{ for discs in } \mathbb{R}^2 \text{ [23,24,30]} \\
\zeta_2(p) \simeq \frac{2}{3}p + \tfrac{1}{3} \text{ for (discs)}^c \text{ in } \mathbb{R}^2 \\
\zeta_1(p) \simeq 0.5057p + 0.2274 \text{ for Poisson polygons in } \mathbb{R}^2 \text{ [23,24]} \\
\zeta_2(p) \simeq 0.5057p + 0.2669 \text{ for (Poisson polygons)}^c \text{ in } \mathbb{R}^2.
\end{gathered} \tag{8}$$

For the models presented in equations (8), we have $\zeta_2(p) > \zeta_1(p)$, so that in the real case, the third order bounds increase when the largest permittivity is attributed to the set A^c. This is due to the fact that it is easier for the "matrix" phase A^c to percolate than for the overlapping inclusions building A. For the sphere and disc models, $\zeta_2(p)$ is larger than the $\zeta_1(p)$ of the corresponding mosaic models.

4.1.3. The Dead Leaves Model. — The dead leaves model [4–6] is obtained sequentially by implantation of random primary grains $A'(t)$ on a Poisson point process: in every point x is kept the last occurring value $\epsilon(x,t)$ during the sequence. In this way, non symmetric random sets are obtained if two different families of primary grains are used for A and for A^c.

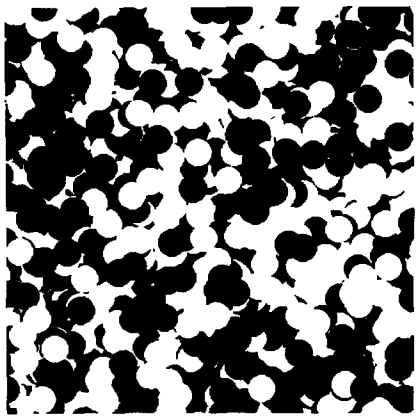


Fig. 10.



Fig. 11.

Fig. 10. — Two phase dead leaves model of discs ($p = 0.5$).

Fig. 11. — Section of a dead leaves model of Poisson polyhedra ($p = 0.5$).

When using the same family of primary grains for the two sets, a mosaic model built on a random tessellation is obtained (Figs. 10 and 11). The shape of the resulting cell is non convex (and even non connected!), due to the overlaps occurring during the construction of the model. For the symmetric case, the calculation of G can be made from the knowledge of the function $s(x, y, \theta)$:

$$s(|h_1|, |h_2|, \theta) = \frac{\overline{\mu}_d(\mathrm{A}' \cap \mathrm{A}'_{h_1} \cap \mathrm{A}'_{h_2})}{\overline{\mu}_d(\mathrm{A}' \cup \mathrm{A}'_{h_1} \cup \mathrm{A}'_{h_2})}.$$

Calculations were made for Poisson polyhedra as primary grains (Fig. 11) [23,24]: $G \simeq 0.170$ in $\mathbb{R}^3$ and $G \simeq 0.311$ in $\mathbb{R}^2$, which is slightly larger than for the Poisson mosaic.

4.2. Combination of Basic Random Sets. — Combining the previous basic models provides more complex structures [23]. For instance, fluctuations of morphological properties (such as the local volume fraction of one phase, p) may exist in real materials. Experimental evidence of such fluctuations was noticed in [31,32] for polymers filled with conducting particles clustering, or in [33,34] for composite materials containing carbon black aggregates percolating for a volume fraction as low as 2-3%. The combination of the random sets presented before can describe such fluctuations. We will use in this hierarchical approach random structures with very different scales, for which an approximate value of $\zeta_1(p)$, noted $\zeta_{H_1}(p)$, can be obtained.

We have to notice that formulae presented in the following subsections are accurate for the combinations of random sets with widely separate scales. The figures illustrating these types of structures very roughly represent this scale separation.

4.2.1. Union and Intersection of Random Sets. — A first way to combine random sets is to consider the union or the intersection of two independent random sets A_1 and A_2. Since we have $(\mathrm{A}_1 \cup \mathrm{A}_2)^c = \mathrm{A}_1^c \cap \mathrm{A}_2^c$, we can limit our purpose to the intersection. For this model, $p = p_1 p_2$ and $P(\mathrm{K}) = P\{\mathrm{K} \subset (\mathrm{A}_1 \cap \mathrm{A}_2)\} = P\{\mathrm{K} \subset \mathrm{A}_1\} P\{\mathrm{K} \subset \mathrm{A}_2\}$. When using the same type of random set ($\zeta_1(p) = \alpha p + \beta$) for the two primary structures (with the scale of A_2 being

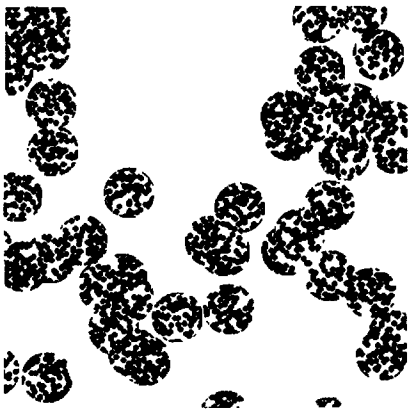


Fig. 12.

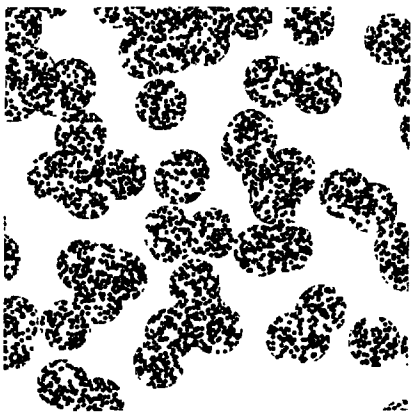


Fig. 13.

Fig. 12. — Intersection of two Boolean models of discs with $p = 0.25$, $p_1 = 0.40$ and $p_2 = 0.62$.

Fig. 13. — Intersection of two Boolean models: $p = 0.25$, $p_1 = p_2 = 0.5$.

much smaller than the scale of A_1), we get the following approximate result:

$$pq\,(\zeta_{H_1}(p) - \zeta_1(p)) = \frac{p^2}{p_1^2}(p_1 - p)(1 - p_1)(\alpha - \beta)$$

and for the two scale model $\zeta_{H_1}(p) > \zeta_1(p)$ when $\alpha \geq \beta \geq 0$. This is the case when the basic model is a mosaic model with $a < 1/3$ or when it is one of the studied Boolean models (or its complementary set).

An optimal value of the increment $\zeta_{H_1}(p) - \zeta_1(p)$ when varying p_1 for a given p, is reached for $p_1 = 2p/(1 + p)$ when $\alpha \geq \beta \geq 0$:

- for the intersection of two Boolean models (Fig. 12) (or of their complementary sets) $\zeta_{H_1 \mathrm{opt}}(p) = p\dfrac{3\alpha + \beta}{4} + \dfrac{3\beta + \alpha}{4}$;
- for the two scale mosaic model with $a < 1/3$, it becomes

$$\zeta_{H_1 \mathrm{opt}}(p) = p\frac{3 - 5a}{4} + \frac{a + 1}{4}$$

A last combination of structures is obtained for $p_1 = p_2$ (Figs. 13 and 14) and for widely separate scales. In that particularly case, we have $p = p_1^2$ and

$$\zeta_{H_1}(p) \simeq \zeta_1(p_1) = \frac{1 + p}{1 + p^{1/2}}\zeta_1(p^{1/2}).$$

By iteration at order n, we have $p = p_1^n$ and

$$\zeta_{H_1}^{(n)}(p) \simeq \frac{1 + p}{1 + p^{1/n}}\zeta_1(p^{1/n})$$

since $p^{1/n} \geq p$, we get $\zeta_{H_1}^{(n)}(p) \geq \zeta_1(p)$ and $\zeta_{H_1}^{(n+1)}(p) \geq \zeta_{H_1}^{(n)}(p)$ if $\zeta_1(p) = \alpha p$ with $\alpha > 0$.

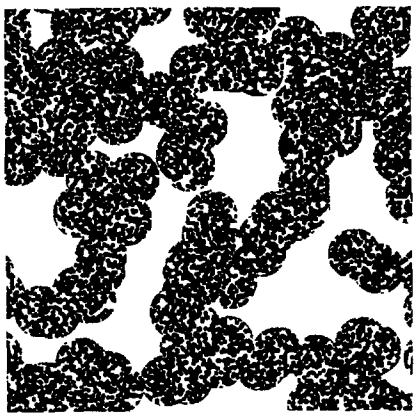


Fig. 14.

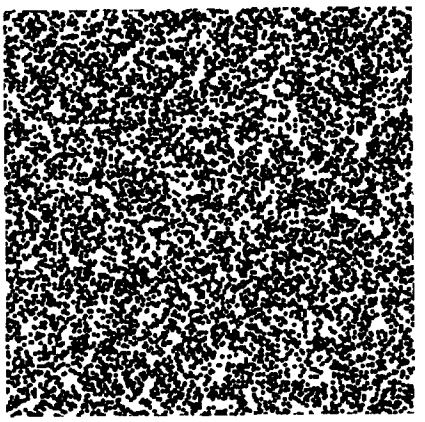


Fig. 15.

Fig. 14. — Intersection of two Boolean models: $p = 0.49$, $p_1 = p_2 = 0.70$.

Fig. 15. — Boolean model of discs with $p = 0.49$.

A limiting case is obtained by iterations for $n \to \infty$:

$$\zeta_{H_1}^{(n)}(p) \to \frac{1+p}{2}\zeta_1(1).$$

If the basic random set is the complementary set of a Boolean model of spheres in $\mathbb{R}^3$ or of discs in $\mathbb{R}^2$, we obtain $\zeta_{H_1}^{(n)}(p) \to (1+p)/2$. This corresponds to a Boolean model of spheres with an infinite range of widely separate sizes.

This last example limited to the first iteration (intersection of two random sets) shows the importance of such a hierarchical model. When $p_1 = 1$ and $p_2 = p$, we recover the standard Boolean model, with a percolation threshold close to 0.6. In Figure 14 is given a simulation of a composite material with a particle volume fraction p equal to 0.49 (with $p_1 = p_2 = 0.7$, $p = p_1 p_2 = 0.49$). The particle phase percolates in this case, while it does not percolate at the same volume fraction ($p = 0.49$) for a standard Boolean model (as in Fig. 15). It is interesting to notice that the new random set obtained after 10 iterations of intersections has a percolation threshold roughly estimated to 0.6%. It is therefore easy to generate in this way interesting microgeometrical media with performant expected properties at low volume fractions.

4.3. A Hierarchical Model. — A simple hierarchical model with two separate scales is built in two steps [6]:

- we start with a primary random tessellation of space into cells,
- every cell is intersected by a realization of a secondary random set (with $\zeta_1(p)$, and with random parameters). Realizations in separate cells are independent.

Any random tessellation can be used in this construction. Any type of random set (mosaic model, Boolean model, dead leaves model, etc...) can be used in the second step.

An example of simulation of a hierarchical model is presented in Figure 16. This model starts from a Poisson tessellation of the space into cells. The density of the Poisson tessellation

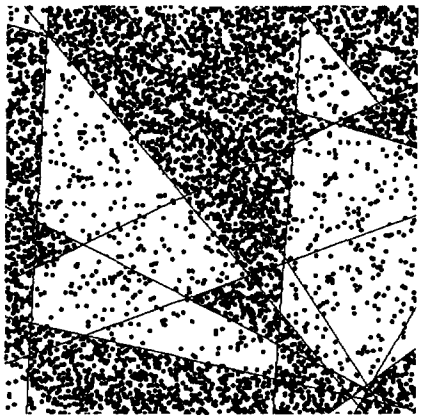


Fig. 16. — Simulation of a hierarchical model.

is $\lambda = [\text{Line number}/(\text{Image size} * \pi * \sqrt{2})]$ (in our example, Line number = 15). Each cell is intersected by a Boolean model of discs, with the density d (probability 0.5) or $5d$ (probability 0.5). As for Figure 6, the lines of the tessellation are absent from the final structure). This simulation of a two scale random set can represent a two phase material with an average particle volume fraction equal to 0.3 presenting local fluctuations of the volume fraction generated by the changes in density (average number of Poisson germs per unit area) from cell to another of the Poisson tessellation.

For cells much larger than the scale of the secondary random set, implanted with a random volume fraction P (with expectation $E\{P\} = p$ and variance $D^2\{P\}$), the function $\zeta_{H_1}(p)$ corresponding to the hierarchical model is approximated by:

$$pq\zeta_{H_1}(p) = E\{P(1-P)\zeta_1(P)\} + pD^2\{P\} + aE\{(P-p)^3\}. \tag{9}$$

Equation (9) recovers $\zeta_1(p)$ when P is non random ($\zeta_{H_1}(p) = \zeta_1(p)$), and the mosaic result (Eq. (7)) when $P = 1$ with the probability p and $P = 0$ with the probability q.

It is interesting to examine the case where $P = p_1$ with the probability p_2 and $P = 0$ with the probability $1 - p_2$: it means that a proportion p_2 of cells is filled with a mixture of A_1 (in a proportion p_1) and A_2 (in a proportion $1 - p_1$), and a proportion $1 - p_2$ of cells is filled with the phase A_2 alone. For this example, $p = p_1 p_2$ (p is the volume fraction of phase 1 *i.e.* A_1 in the final material). If $\zeta_1(p) = \alpha p + \beta$ (which is the case of mosaic models, and approximately the case of Boolean models), equation (9) becomes:

$$pq\,(\zeta_{H_1}(p) - \zeta_1(p)) = p(p_1 - p)\,(p(1-3\alpha) + \alpha - \beta + (p_1 - 2p)(a - \alpha))\,.$$

We can consider now situations where the increment $\zeta_{H_1}(p) - \zeta_1(p)$ reaches an optimal value $\zeta_{H_1 \text{opt}}(p)$ when varying p_1 for a given p. It can admit a positive optimum when $a < \alpha$, for $p_1 = \frac{p(1-3a)+\alpha-\beta}{2(a-\alpha)}$.

$$\zeta_{H_1 \text{opt}}(p) - \zeta_1(p) = \frac{(p(a+2\alpha-1)+\beta-\alpha)^2}{4q(\alpha-a)}$$

For instance, when the secondary random set is a mosaic model built up on the same type of tessellation as the primary random tessellation (but on a much smaller scale), the increment is always positive $\zeta_{H_1}(p) - \zeta_1(p) > 0$ for $a < 1/3$ (that is for $G < 1/3$ in $\mathbb{R}^2$ and $G < 5/27$

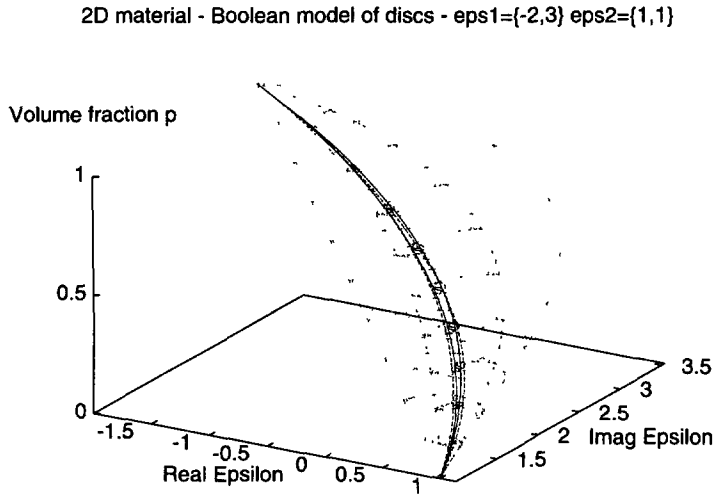


Fig. 17. — Regions Ω^n $(n = 0, .., 4)$ of the complex plane filled by the values of ϵ_e when p varies.

in $\mathbb{R}^3$). In these conditions, the two scales model provides different bounds than the initial one scale mosaic (higher bounds in real case). And, for $p_1 = (p+1)/2$:

$$\zeta_{H_1 \mathrm{opt}}(p) = p\left(\frac{3-5a}{4}\right) + \frac{a+1}{4}$$

This result is the same as for the intersection of two independent random mosaics presented in Section 4.2.1, and obtained for a different construction: the two types of models cannot be distinguished when restricting up to third order correlation functions.

5. Examples of Regions of the Complex Dielectric Permittivity of Random Media

First of all, Figure 1 describes the complex bounds Ω^n on the effective permittivity ϵ_e for different orders $(n = 0, .., 4)$ and for one volume fraction p. These regions Ω^n vary with p. So, the representation of these bounds in a three-dimensional graph $(\epsilon', \epsilon'', p)$ looks like spindles. Figure 17 gives an example of such spindles that are narrower when increasing the order of correlation functions.

In what follows, we will generally consider only the higher available order; which means third order in 3D models, and fourth order in 2D models.

We consider first the fourth order regions of ϵ_e in the **two dimensional space** at changing volume fraction p and for different random models.

- *For a Boolean material* of discs (the discs having the permittivity ϵ_1), we see in Figure 18 that the domains obtained by exchanging the geometry of the two phases are separate: the real part of ϵ_e is expected to become negative for a lower volume fraction when ϵ_1 is affected to the complementary set of the union of discs. For Poisson polygon grains (the grains having the permittivity ϵ_1), the functions $\zeta_1(p) \simeq \zeta_2(p)$ and the resulting domains are similar (Fig. 19).

- *For the mosaic model*, the symmetry of the domains with respect to the probability p appears in Figure 20, where it is clear that when $p = 0.5$, the domains are the same whatever the mosaic since $\zeta_1(0.5) = 0.5$. In two dimensions, it encloses the geometrical mean when $p_1 = 0.5$.

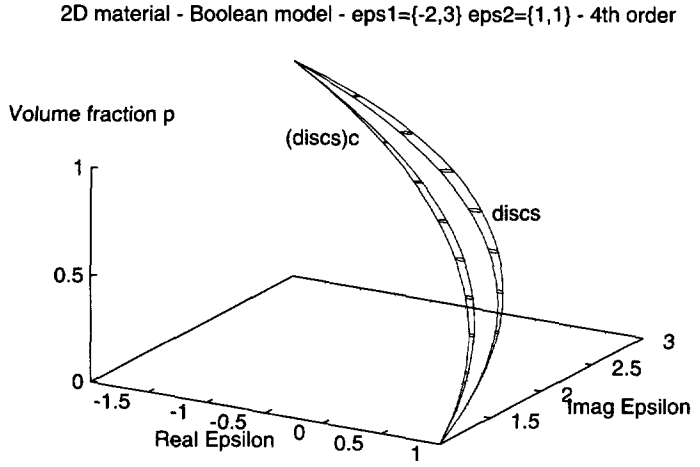


Fig. 18. — 4th order bounds for Boolean models of discs and $(\text{discs})^c$.

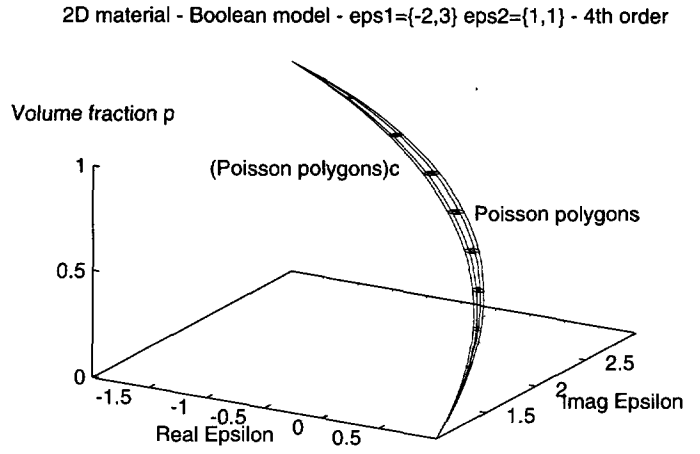


Fig. 19. — 4th order bounds for the Boolean model of Poisson polygons and $(\text{Poisson polygons})^c$.

The anisotropy of primary grains is a parameter of great interest. Figures 20 and 21 show isotropic grains like discs, providing bounds similar to the cases of squares or Poisson polygons. Anisotropic grains like rectangles with an important side ratio ($L = 200$) or needles, give bounds separated from the case of the isotropic cells.

- *For the dead leaves model* in Figure 22, squares and elongated rectangles provide separate domains (but closer than for the cell model).
- It is also possible to compare different models built with the same primary grains, like the Boolean and the mosaic models of discs (Fig. 23). Their behavior is different since the Boolean model is not symmetric.

In the **three dimensional space**, we are limited to the third order domains.

- *For the Boolean model* of spheres in Figure 24, where the exchange of the morphology of the two phases (ϵ_1 being first assigned to the grains, and then to the complementary set) gives separate domains. The same qualitative behavior as for the 2D case is observed.

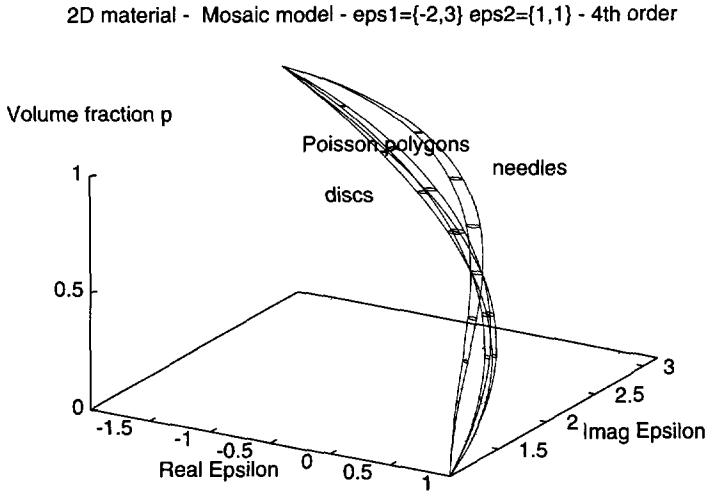


Fig. 20. — 4th order bounds for mosaic models of discs, Poisson polygons, and needles.

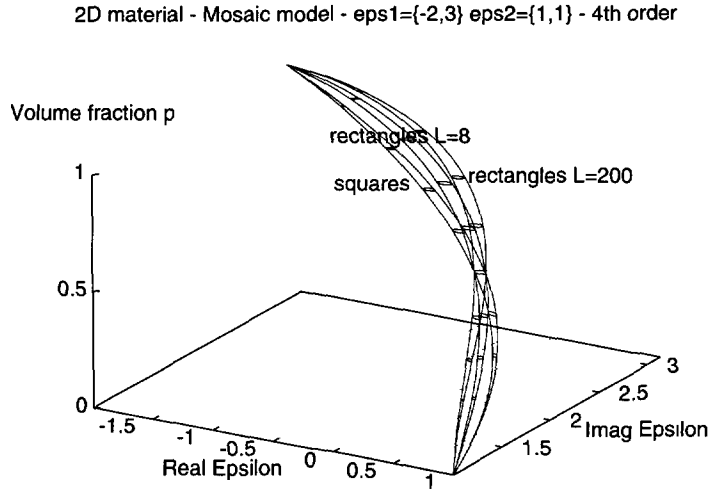


Fig. 21. — 4th order bounds for mosaic model of squares, rectangles ($L = 8$), and rectangles ($L = 200$).

- Figure 25 illustrates the evolution of effective properties when iterating the *intersection of Boolean models* of spheres with the same volume fraction ($p = p_1^n$), the grains having the permittivity ϵ_1. These random sets are described in Section 4.2.1 and Figures 13 and 14 illustrate their construction. The complex bounds are represented for two volume fractions $p = 0.25$ and 0.50. In this example, they provide almost separate domains in the complex plane when $p = 0.25$.

- Figure 26 shows the effective properties of optimized *hierarchical models* compared with the one scale mosaic model. They produce separate domains in the complex plane, leading to different permittivities for these different textures.

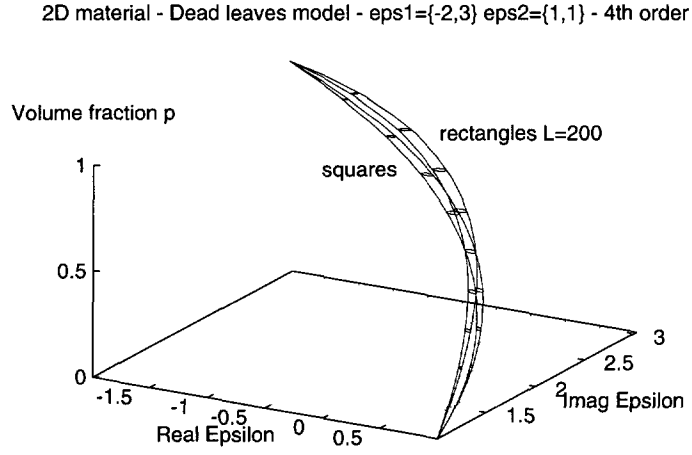


Fig. 22. — 4th order bounds for dead leaves models of squares and rectangles ($L = 200$).

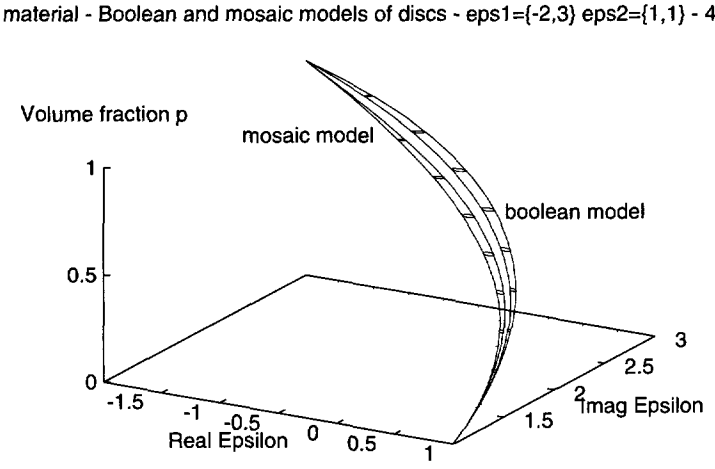


Fig. 23. — 4th order bounds for Boolean and mosaic models of discs.

To summarize these results, we can build models of random composites, for which the effective complex permittivity lays in domains in the complex plane which are more accurate than what can be obtained from the isotropic assumption: everything being constant (properties ϵ_1 and ϵ_2 of the phases, volume fraction p of the set A), the effective property reaches the point A^2 when $\zeta_1(p) \to 1$, and the point B^2 when $\zeta_1(p) \to 0$; therefore, increasing the value of $\zeta_1(p)$ brings the effective property close to A^2 in the complex plane; this is obtained by acting on the following morphological criteria: by increasing the anisotropy of the random primary grain (Boolean model whatever p, dead leaves and mosaic models for $p < 0.5$), by affecting the property ϵ_1 to the complementary set of the primary grains for Boolean models, and more generally by developing a microstructure with a lower percolation threshold for the phase with the property ϵ_1 (as obtained for the intersection of Boolean random sets).

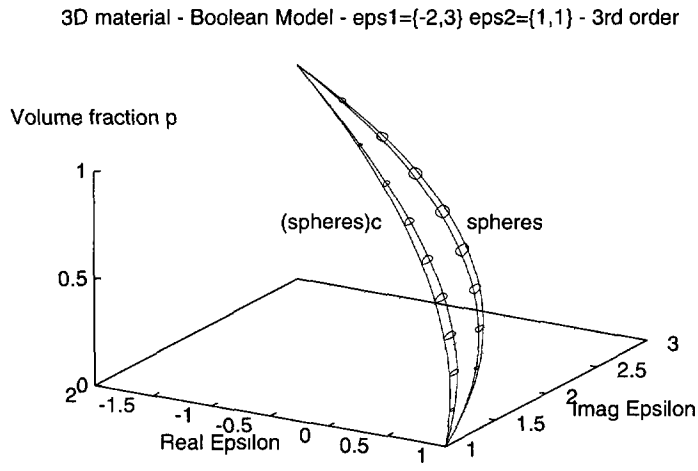


Fig. 24. — 3rd order bounds for the Boolean model of spheres and $(\text{spheres})^c$.

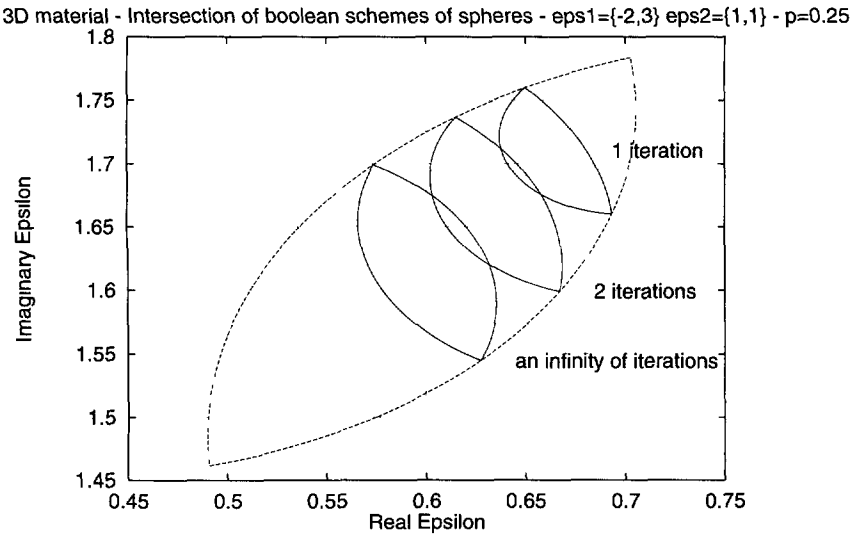


Fig. 25. — Bounds for the intersection of Boolean models of spheres (2nd and 3rd orders).

6. Conclusion

Models of random structures can provide different bounds of the effective properties, even when considering the third order (3D) or the fourth order (2D) bounds. A similar approach can be followed to predict the frequency dependency of the complex permittivity. for a frequency range which is in agreement with the scale of the microstructure, frequency dependent domains can be obtained in the complex plane. Therefore, useful information on the choice of the microstructure can be obtained in this way.

The models introduced in this paper have a multiphase and even a continuous version (scalar or multivariate) [5, 6], for which the calculation of third order bounds in the real case can be made using the general derivation based on the third order correlation function [7, 10, 27].

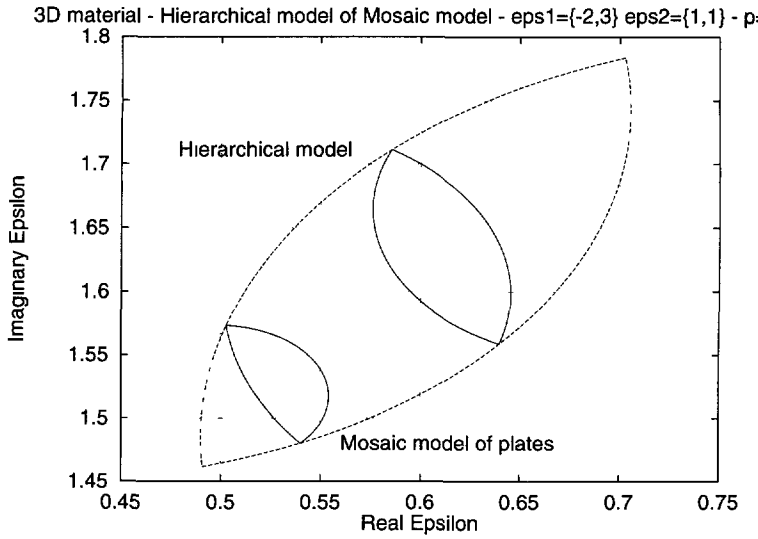


Fig. 26. — Bounds for a hierarchical model of mosaic with plate cells (2nd and 3rd orders).

The extension of these more general textures to the complex permittivity requires further theoretical developments.

Acknowledgments

A part of this study was made with the financial support of DRET (contract 92 017 00 025). Laurent Savary is also grateful to CNRS and DRET for a grant.

References

[1] Matheron G., Eléments pour une théorie des milieux poreux (Masson, Paris, 1967).
[2] Matheron G., Random sets and integral geometry (J. Wiley, New York, 1975).
[3] Serra J., Image analysis and mathematical morphology (Academic Press, London, 1982).
[4] Jeulin D., in: Proc. CMDS5, A.J.M. Spencer, Ed. (Balkema, Rotterdam, 1987) p. 217.
[5] Jeulin D., Thèse de Doctorat d'État, University of Caen (1991).
[6] Jeulin D., Morphological models of random structures (CRC press, in preparation).
[7] Beran M.J., Statistical Continuum Theories (J. Wiley, New York, 1968).
[8] Kröner E., Statistical Continuum Mechanics (Springer Verlag, Berlin. 1971).
[9] Hashin Z. and Shtrikman S., *J. Appl. Phys.* **33** (1962) 3125.
[10] Hori M., *J. Math. Phys.* **14** (1973) 1942.
[11] Milton G.W., *J. Appl. Phys.* **52** (1981) 5294.
[12] Milton G.W., *J. Mech. Phys. Solids* **30** (1982) 177.
[13] McPhedran R. and Milton G., *Appl. Phys.* **A26** (1981) 205.
[14] McPhedran R., McKenzie R., Milton G., *Appl. Phys.* **A29** (1982) 19.
[15] Jeulin D. and Savary L., accepted for publication in *Physica A.*

[16] Beran M.J., *Il Nuovo Cimento* **38** (1965) 771.
[17] Milton G.W., *Appl. Phys. Lett.* **37** (1980) 300.
[18] Bergman D.J., *Phys. Rep.* **43C** (1978) 377.
[19] Keller J.B., *J. Math. Phys.* **5** (1964) 548.
[20] Dykhne A.M., *Zh. Eksp. Teor. Fiz.* **59** (1970) 110.
[21] Mendelson K.S., *J. Appl. Phys.* **15** (1975) 917.
[22] Milton G.W., *Phys. Rev. Lett.* **46** (1981) 542.
[23] Jeulin D. and Le Coënt A., in "Continuum Models of Discrete Systems", K.Z. Markov, Ed. (World Scientific Publishing Company, 1996) p. 1996.
[24] Le Coënt A. and Jeulin D., *C. R. Acad. Sci. Paris Ser. IIb* **323** (1996) 299.
[25] Andraud C., Thèse de Doctorat de l'UPMC (1996).
[26] Matheron G., *Rev. IFP* **23** (1968) 201.
[27] Miller M., *J. Math. Phys.* **10** (1969) 1988.
[28] Torquato S. and Stell G., *J. Chem. Phys.* **79** (1983) 1505.
[29] Torquato S. and Lado F., *Phys. Rev. B* **33** (1986) 6428.
[30] Joslin C. and Stell G., *J. Appl. Phys.* **60** (1986) 1607.
[31] Carmona F., *Physica A* **157** (1989) 461.
[32] Meraoumia T., Thèse de l'Université Bordeaux I (1994).
[33] Michels M.A.J., Brokken-Zijp J.C.M., Groenewoud W.M. and Knoester A., *Physica A* **157** (1989) 529.
[34] Le Coënt A., Thèse de l'ENSMP (1995).